

32 ¹⁴Shenzhen Bay Laboratory, Shenzhen 51800, China

33 ¹⁵These authors contributed equally

34

35 *Correspondence: xuxun@genomics.cn (X.X.), huyong@genomics.cn (Y.H.),

36 miguel@gibh.ac.cn (M.A.E.), liulongqi@genomics.cn (L.L.)

37

38 **Key words:**

39 Single-cell transcriptomics, non-human primate, COVID-19, SARS-CoV-2, ACE2, TMPRSS2,

40 kidney, Interleukin 6, STAT transcription factors, immune cell exhaustion

41

42 **Bullet points:**

43 1-We generated a single-cell transcriptome atlas of 9 monkey tissues to study COVID-19.

44 2-*ACE2*⁺*TMPRSS2*⁺ epithelial cells of lung, kidney and liver are targets for SARS-CoV-2.

45 3-*ACE2* correlation analysis shows *IDO2* and *ANPEP* as potential therapeutic opportunities.

46 4-We unveil a link between IL6, STAT transcription factors and boosted SARS-CoV-2 entry.

47

48

49 **ABSTRACT**

50

51 Stopping COVID-19 is a priority worldwide. Understanding which cell types are targeted by
52 SARS-CoV-2 virus, whether interspecies differences exist, and how variations in cell state
53 influence viral entry is fundamental for accelerating therapeutic and preventative
54 approaches. In this endeavor, we profiled the transcriptome of nine tissues from a *Macaca*
55 *fascicularis* monkey at single-cell resolution. The distribution of SARS-CoV-2 facilitators, ACE2
56 and TMRPSS2, in different cell subtypes showed substantial heterogeneity across lung,
57 kidney, and liver. Through co-expression analysis, we identified immunomodulatory proteins
58 such as IDO2 and ANPEP as potential SARS-CoV-2 targets responsible for immune cell
59 exhaustion. Furthermore, single-cell chromatin accessibility analysis of the kidney unveiled a
60 plausible link between IL6-mediated innate immune responses aiming to protect tissue and
61 enhanced ACE2 expression that could promote viral entry. Our work constitutes a unique
62 resource for understanding the physiology and pathophysiology of two phylogenetically close
63 species, which might guide in the development of therapeutic approaches in humans.

64

65 INTRODUCTION

66

67 As the distance between humans and wild animal habitats diminishes due to uncontrolled
68 human expansion, a series of zoonotic diseases with high mortality rates have emerged. For
69 instance, the recent outbreak of Ebola in Africa, which killed over 5,000 people, was most
70 likely spread from bats and primates to humans¹. The current outbreak of coronavirus disease
71 2019 (COVID-19) caused by the coronavirus severe acute respiratory syndrome coronavirus 2
72 (SARS-CoV-2)² is not the only example of coronaviruses that have recently passed from
73 animals to humans. Coronaviruses are a family of RNA viruses that typically cause respiratory
74 tract infections in humans, yet they are frequently in the reservoir of wild animals with no
75 disease³. For example, the common cold is often (10-15%) caused by a coronavirus (e.g. HCoV-
76 229E and HCoV-OC43)⁴. However, coronaviruses can also lead to severe and life-threatening
77 diseases. In the early 2000s a coronavirus called SARS-CoV, believed to be passed from bats
78 to humans in South East Asia, caused more than 700 deaths from around 8,000 confirmed
79 cases worldwide⁵. Since 2012, another zoonotic coronavirus believed to have passed from
80 camels to humans in the Middle East was designated as Middle East Respiratory Syndrome
81 (MERS)⁶. To date, there have been over 2,500 confirmed cases of MERS with over 800 deaths.
82 While SARS appears to have been eradicated, MERS cases are sporadic and human to human
83 spread is limited⁴.

84 As of 21st April 2020, COVID-19² has become a global pandemic with more than
85 ~2,500,000 confirmed cases and over 170,000 deaths. Due to its high infectivity rate and the
86 high level of intensive care that many patients need, COVID-19 has overwhelmed national
87 health services and destabilized the world. One important reason is that many people who
88 are positive for the virus show mild symptoms^{7, 8}, leading to unnoticed spread of the virus.
89 The current worldwide emergency, possibility of continued expansion to less developed
90 countries, risk of virus mutations and the perpetuation beyond this season has made it
91 imperative to stop the trajectory of virus spreading. Developing drugs and preventative
92 vaccines are ongoing but to warrant success it is necessary to have more knowledge about
93 the disease mechanisms. So far, little is known except for the viral binding via angiotensin
94 converting enzyme 2 (ACE2) and subsequent priming by type 2 transmembrane serine
95 protease 2 (TMPRSS2) protease, which are shared mechanisms with SARS and MERS^{9, 10}. To
96 test experimental treatments, animal models close to humans are necessary due to sequence

97 variation of ACE2 and changes in the proportions of cell subtypes in organs between species.
98 For these reasons, it is essential to have a species close to human to study COVID-19. In this
99 regard, monkey experiments have shown that infection with SARS-CoV-2 produces clinical
100 manifestations similar to COVID-19 patients¹¹. Another study demonstrated that infection
101 with SARS-CoV-2 in monkeys is preventable by acquired immunity, answering one of the
102 outstanding questions about the disease¹².

103 Issues about the proportions of cell types within organs between species and their
104 crosstalk can be addressed effectively through single-cell profiling technologies, in particular
105 single-cell RNA-sequencing (RNA-seq) and single-cell assay for transposase accessible
106 chromatin-sequencing (ATAC-seq). Yet, although human data are accumulating¹³, monkey
107 data are still scarce. The comparison between human and monkey data will be crucial for
108 advancing our knowledge of COVID-19. Here, we provide a high-resolution single-cell atlas of
109 nine organs/tissues (lung, kidney, pancreas, brain, parotid, liver, thyroid, aorta artery, and
110 blood) in monkey, encompassing 215,334 cells. By comparing the expression of SARS related
111 targets in monkey and human, we have identified cell-to-cell similarities as expected.
112 Crucially, we also discovered stark differences in *ACE2* expression between these two species,
113 for example in the ciliated vs pulmonary alveolar type 2 cells of the lung and hepatocytes in
114 liver. We also observed that *ACE2* is heterogeneous among different epithelial cell subtypes
115 across these organs/tissues, suggesting that variations in cell state could influence viral entry.
116 Supporting this, single-cell ATAC-seq of monkey kidney identified regulatory elements driven
117 by signal transducer and activator of transcription factor 1 and 3 (STAT1 and 3) and interferon
118 regulatory factor 1 (IRF) in the *ACE2* locus. This suggests that cytokines, particularly
119 interleukin 6 (IL6), aiming to induce a tissue protective response can exacerbate the disease
120 by aiding viral entry into target cells. Additionally, through correlation analysis with *ACE2*
121 expression, we have identified several potential candidates involved in COVID-19
122 pathophysiology, such as Transmembrane protein 27 (TMEM27), Indoleamine 2,3-
123 dioxygenase 2 (IDO2), DnaJ heat shock protein family (Hsp40) member C12 (DNAJC12) and
124 Alanyl aminopeptidase N (ANPEP). These targets may offer therapeutic opportunities.

125 Taken together, our data constitute a unique resource which could aid the scientific
126 community in the fight against SARS-CoV-2. From a wider perspective, this will also be
127 instrumental for systematic comparative studies aimed at understanding physiological and
128 pathophysiological differences between monkey and other species, in particular, human.

129

130 RESULTS

131

132 Cellular heterogeneity of nine non-human primate tissues assessed by single-cell RNA-seq.

133 We profiled, at the single-cell level, the transcriptome of the model organism cynomolgus
134 monkey (*Macaca fascicularis*), as it is phylogenetically close to human and this could help
135 advance our knowledge of human physiology and disease. As proof of principle, we decided
136 to use our data to understand what cell types are mainly targeted by SARS-CoV-2 and how
137 this could trigger the clinical features that have been lethal in a number of patients. For this
138 study, we used a six-year-old female monkey in which we profiled nine different organs (**Fig.**
139 **1a**). These included lung, liver and kidney as the known affected organs by the closely related
140 SARS-CoV infection¹⁴, and have been reported to have high *ACE2* expression in human¹⁵.
141 Peripheral blood mononuclear cells (PBMC) were added because altered immune responses
142 are thought to be detrimental in the disease¹⁶. Neocortex was chosen because of the clinical
143 symptoms which involve loss of smell and taste suggesting that the central nervous system
144 may be targeted¹⁷. The parotid gland was chosen on the basis that saliva is one of the main
145 means of infection spread. Additionally, we selected aorta, thyroid and pancreas.

146 We employed a high-throughput platform recently developed in-house, DNBelab C4,
147 which is a scalable and cost-effective approach for microfluidic droplet-based approach¹⁸.
148 Except for PBMC sequencing, which was performed using cells in suspension, the sequencing
149 for all the other organs was done using single-nucleus library preparations. Following
150 euthanasia, the selected organs were extracted, single-nucleus/cell suspensions were
151 obtained and then used for library preparation. A total of 40,226 liver, 45,286 kidney, 36,421
152 pancreas, 44,355 parotid gland, 12,822 lung, 7,877 thyroid, 6,361 neocortex, 2,260 aorta
153 nuclei and 19,726 PBMCs passed quality control and were used for downstream analysis
154 (**Extended Data Fig. 1a, b, Supplementary Table 1**).

155 In a global view of our single-cell dataset, each organ clustered separately, with the
156 exception of a few cell types such as macrophages, adipocytes and endothelial cells, which
157 were shared between different organs (**Fig. 1b**). We performed Uniform Manifold
158 Approximation and Projection (UMAP) on the 215,334 cells and identified 44 major clusters
159 by performing unbiased graph-based Louvain clustering (**Supplementary Table 1**). Some
160 clusters were largely composed of cells belonging to a specific tissue, such as hepatocytes in

161 cluster 13, pancreatic acinar cells in cluster 26 and parotid acinar cells in cluster 30 (**Fig. 1c**,
162 **Extended Data Fig. 1c**). We next performed clustering and differential gene expression
163 analysis to dissect the cellular composition of each individual organ. These analyses confirmed
164 the typical patterns of cell heterogeneity for all the organs/tissues. When examining the lung
165 tissue, we defined 10 major clusters with specific molecular markers, including ciliated cells,
166 macrophages, cycling macrophages, smooth muscle cells, fibroblasts, pericytes, pulmonary
167 alveolar (pneumocytes) type 1 and type 2, endothelial and club cells (**Extended Data Fig. 2a**).
168 The kidney consisted of 11 clusters, those being podocytes, thick ascending limb cells,
169 proximal tubule cells, intercalated cells 1 and 2, connecting tubule cells, distal convoluted
170 tubule cells, stomal cells, thin limb cells, principal cells and endothelial cells (**Extended Data**
171 **Fig. 2b**). Analysis of liver tissue revealed hepatocytes to be the larger cell population, while
172 other clusters consisted of cholangiocytes, macrophages (Kupffer cells), natural killer-T (NK-
173 T) cells, endothelial cells and hepatic stellate cells (**Extended Data Fig. 2c**). Inspection of PBMC
174 clustering revealed large populations of B cells, CD4⁺, CD8⁺ naïve and CD8⁺ memory T cells,
175 together with smaller populations of natural killer (NK) cells, dendritic cells, CD16⁺ and CD14⁺
176 monocytes (**Extended Data Fig. 2d**). Likewise, the neocortex contained excitatory neurons,
177 astrocytes, microglia, parvalbumin (PVALB), somatostatin-expressing neurons (SST), synaptic
178 vesicle glycoprotein-expressing cells (SV2C), vasoactive intestinal polypeptide-expressing
179 neurons (VIP), oligodendrocytes and oligodendrocyte precursor cells (**Extended Data Fig. 2e**).
180 Parotid gland instead was composed of a large cluster of serous acinar cells together with
181 small clusters of macrophages, stromal cells, myoepithelial cells, striated duct cells, mucous
182 acinar cells and intercalated duct cells (**Extended Data Fig. 2f**). Aorta cells could be further
183 divided into adipocytes, endothelial cells, myofibroblasts and a large proportion of smooth
184 muscle cells (**Extended Data Fig. 2g**). Our clustering also demonstrated that most of the
185 thyroid gland is composed of follicular cells, with smaller populations of adipocytes,
186 endothelial cells, stromal and smooth muscle cells (**Extended Data Fig. 2h**). Finally, our data
187 showed the largest population of the pancreas to be acinar cells, while smaller clusters were
188 comprised of stromal, ductal, and islet cells (alpha and beta), together with a population that
189 could not be assigned to any known cell type (**Extended Data Fig. 2i**).

190 In conclusion, we have successfully profiled the transcriptome of nine organs at single-
191 cell resolution in monkey, which could assist in the study of COVID-19.

192

193 ***ACE2* and *TMPRSS2* single-cell expression landscape in a non-human primate.**

194 Recent studies have reported that, similarly to SARS-CoV, the capacity of SARS-CoV-2 virus to
195 infect host cells relies on viral spike (S) protein binding to ACE2 entry receptor^{9, 10}, which is
196 involved in the control of blood pressure through the renin-angiotensin system¹⁹. This
197 phenomenon is primed by the multifunction serine protease TMPRSS2²⁰. Accordingly, double
198 positive (*ACE2*⁺/*TMPRSS2*⁺) cells have higher risk of infection by SARS-CoV-2. Although
199 immunohistological studies have demonstrated localization of these two proteins in the
200 respiratory tract²¹, it is unclear which cell subtypes express these genes and how homogenous
201 the expression among a specific cell subtype is. Also, comprehensive information about other
202 cell types and organs that express these two proteins and could be targeted by the virus in
203 human or monkey is lacking.

204 We inspected our data to see how widespread and homogenous *ACE2* expression was
205 in the monkey tissues. As expected, *ACE2* was detected in several lung clusters, mainly ciliated
206 cells, club cells and pulmonary alveolar type 2 cells (**Fig. 2a, 2d, 3a upper panel**), whereas in
207 the kidney, *ACE2* was primarily present in proximal tubule cells (**Fig. 2a, 2d, 3b upper panel**).
208 The latter is consistent with reports describing that a significant number of COVID-19 patients
209 display altered kidney function^{15, 22}. Interestingly, *ACE2* expression was heterogenous among
210 these cell subtypes in both lung and kidney. In the liver, *ACE2* was mostly expressed in
211 cholangiocytes, with a smaller degree of expression also found in hepatocytes (**Fig. 2a, 2d, 3c**
212 **upper panel**). Notably, the closely related SARS-CoV caused liver injury due to hepatitis in
213 some patients²³, suggesting that the liver may also be a direct target for SARS-CoV-2. A small
214 proportion of *ACE2*⁺ was also observed in pancreatic islet cells (**Fig. 2a, 2d, Extended Data Fig.**
215 **3a**). In contrast, little or no expression was observed in thyroid, neocortex, parotid and PBMC
216 (**Fig. 2a, 2d, Extended Data Fig. 3a**). Negligible *ACE2* expression in the neocortex suggests that
217 other tissues may be affected by SARS-CoV-2 that cause loss of taste and smell, regarding the
218 latter in particular the olfactory epithelium.

219 *TMPRSS2* displayed more broadly expressed across cell types in multiple tissues,
220 although it was highest in kidney cells. However, in contrast to *ACE2*, its expression was
221 highest in the distal convoluted tubule, thin limb, intercalated and principal cell 1 and 2 kidney
222 clusters (**Fig. 2b, 2d, 3b lower panel, Extended Data Fig. 3b**). Additionally, significant
223 *TMPRSS2* was observed in both parotid and pancreatic acinar cells, thyroid follicular cells,
224 cholangiocytes and in several lung clusters (**Fig. 2b, 2d, Extended Data Fig. 3**). We then

225 determined which cells co-expressed both genes (*ACE2*⁺/*TMPRSS2*⁺). Notably, the largest
226 overlap between *ACE2* and *TMPRSS2* was observed in the ciliated and club cell clusters of the
227 lung and to a lesser extent the proximal tubule cells of the kidney (**Fig. 2c, 2e**). A smaller
228 overlap was also observed in cholangiocytes and in pancreatic islet cells (**Fig. 2c, 2e**).

229 Therefore, our data show that *ACE2* and *TMPRSS2* are expressed in a variety of cell
230 types, mainly epithelial cells, within the nine monkey organs/tissues (**Supplementary Table**
231 **2a**). The observed heterogeneity of *ACE2* in these cell subtypes also suggests that variations
232 in cell state (e.g. differentiation state, stimulation state or topographical distribution) cause
233 heterogenous expression across an individual tissue. These observations may provide
234 important clues about COVID-19 pathogenesis and symptomatology.

235
236 **Comparative analysis of *ACE2* and *TMPRSS2* expression in human and non-human primate.**

237 Given the heterogeneous nature of *ACE2* and *TMPRSS2* expression within monkey tissues, we
238 decided to investigate similarities and differences between human and monkey. For this
239 purpose, we retrieved publicly available data from single-cell studies in human (see methods).
240 *TMPRSS2* distribution was similar in cell subtypes of lung, kidney and liver between human
241 and monkey (**Fig. 3d-3f**). However, strikingly, *ACE2* showed distinct patterns among cell
242 subtypes in all three organs between the two species (**Fig. 3d-3f**). The biggest differences
243 were observed in ciliated cells of the lung, which had the highest expression of *ACE2* in
244 monkey, and pulmonary alveolar type 2 cells, which had the highest expression of *ACE2* in
245 human. The function of ciliated cells is to move substances (e.g. cell debris and toxic material)
246 across the surface of the respiratory tract and are commonly targeted by respiratory viruses,
247 whereas pulmonary alveolar type 2 cells have regenerative properties, are crucial for alveolar
248 homeostasis and produce surfactant^{24, 25}. In the kidney of both monkey and human, the
249 highest *ACE2* expression was in proximal tubule cells (**Fig. 3e**), which are responsible for
250 electrolyte and nutrient reabsorption. However, renal endothelial cells had higher expression
251 in monkey compared to human. In liver, cholangiocytes had similarly high *ACE2* expression in
252 monkey and human, but hepatocytes showed higher expression and more positive cells in the
253 human (**Fig. 3f**). Considering the heterogenous expression of *ACE2* within the proximal tubule
254 cells in monkey, we revisited the previously analyzed data and were able to sub cluster this
255 population of cells into two (S1 and S3) based on the expression of *SLC5A2* and *SLC7A13*²⁶
256 (**Extended Data Fig. 4, Supplementary Table 2b**). These two genes are sodium and glucose

257 cotransporters involved in glucose reabsorption in the kidney^{27,28}. We did not include thyroid,
258 pancreas or aorta in these analyses because of lack of high-quality available human single-cell
259 datasets. As for the neocortex and PBMC, they have little to no expression of *ACE2* in human
260 (data not shown).

261 These differences in *ACE2* expression across cell subtypes in the lung, kidney and liver
262 in monkey and human raise the possibility that infection with SARS-CoV-2 in the two species
263 will have different effects.

264

265 ***ACE2* correlation analysis across cell types reveals potential therapeutic targets.**

266 To shed light on potential mechanisms that could facilitate *ACE2*-mediated SARS-CoV-2
267 infection, we performed an analysis of the Pearson's correlation coefficient, based on gene
268 expression in the 44 cell subtypes, to determine what genes are co-regulated with *ACE2* in
269 monkey tissues. Correlated genes were considered as those displaying a coefficient higher
270 than 0.6 with an adjusted *P* value < 0.001. Using these criteria, we observed several genes
271 with marked correlation, including genes that belong to metabolic and developmental
272 pathways and genes involved in the cellular response to xenobiotic stimuli (**Fig. 4a, b**). The
273 highest correlation was observed for transmembrane protein 27 (*TMEM27*, cor = 0.84), a
274 protein involved in trafficking amino acid transporters to the apical brush border of kidney
275 proximal tubules²⁹. This is unsurprising considering that *TMEM27* is an important paralog of
276 *ACE2*, and high expression was restricted to kidney cells. DnaJ heat shock protein family
277 (Hsp40) member C12 (*DNAJC12*, cor = 0.78), a gene with a role in immune response
278 processes³⁰, had a distribution like *TMEM27*. Importantly, we also observed high correlation
279 with Indoleamine 2,3-dioxygenase 2 (*IDO2*, cor = 0.77), a gene with abundant expression in
280 kidney and liver cells that was also expressed in the lung and other organs. *IDO2* functions
281 during the early phases of immune responses and promotes inflammatory autoimmunity³¹,
282 ³². *ANPEP*, which encodes for alanyl aminopeptidase N, was also co-expressed with *ACE2* in
283 kidney, liver and to a lesser extent in lung too (cor = 0.64), like *IDO2* (**Fig. 4c, d**). Interestingly,
284 *ANPEP* has also been shown to be participate in immune responses, virus receptor activity
285 and in mediating virus entry into host cells^{33,34}.

286 These data highlight potential therapeutic targets to help in the fight against SARS-
287 CoV-2. Due to their potential co-regulation with *ACE2*, *DNAJC12* and *ANPEP* it is also possible
288 that they modulate and/or are directly involved in viral entry. Alternatively, depletion of cells

289 expressing *IDO2* and *ANPEP* through a cytopathic effect of the virus could trigger an
290 uncontrolled immune response and contribute to the immune cell exhaustion observed in
291 COVID-19³⁵.

292

293 **Epigenetic regulation of *ACE2* in each cell subtype of monkey kidney.**

294 To understand whether epigenetic mechanisms underlie the heterogeneity of *ACE2*
295 expression in the kidney, as representative for other organs, we employed DNBelab C4
296 technology to perform high-throughput single-cell ATAC-seq (**Fig. 5a**). After filtering, 6,353
297 nuclei were used for downstream analysis (**Extended Data Fig. 5a, b, Supplementary Table**
298 **4**). We integrated these data with the kidney transcriptomic data described in **Fig. 1** and
299 proceeded to perform Louvain clustering to map all the different cell types within the dataset
300 (**Fig. 5b**). Consistent with the transcriptomic data, our epigenomic mapping identified thick
301 ascending limb cells and proximal tubule cells as the largest kidney clusters (**Extended Data**
302 **Fig. 2b**). Similarly, smaller clusters of podocytes, principal, intercalated, connected tubule,
303 distal convoluted tubule, thin limb, endothelial and stromal cells were detected (**Fig. 5c,**
304 **Extended Data Fig. 5c**). Analysis of open chromatin regions revealed discrete peaks in the
305 *ACE2* locus, with the highest signal detected in proximal tubule cells S1 and S3, which are also
306 the highest *ACE2*-expressing cells (**Fig. 5d**). Our approach failed to detect significant signal
307 enrichment in the *ACE2* locus in endothelial cells, possibly related to the low level of
308 expression (**Fig. 5d**). Within the cells of the kidney we observed the highest percentage of
309 *ACE2*⁺ cells in the proximal tubule S3, with a lower percentage in the proximal tubule S1 and
310 endothelial cells (**Fig. 5e**). Motif analysis within the open chromatin regions in *ACE2*⁺ cells
311 demonstrated that these regions were preferentially enriched in STAT1 and 3 and IRF1
312 binding sites (**Fig. 5f**). These findings suggested that tissue protective cytokines including IL5,
313 IL6, EGF and interferons are acting on these proximal tubule cells S3 to induce *ACE2*. We
314 focused on IL6 because a recent clinical trial has been started that uses anti-IL6 receptor (IL6R)
315 antibodies in the treatment of COVID-19
316 (<http://www.chictr.org.cn/showprojen.aspx?proj=49409>). IL6 is a potent regulator of
317 immune responses and can be produced by a variety of interstitial cells including fibroblasts,
318 endothelial cells and more importantly tissue macrophages³⁶. Interestingly, we also noticed
319 that distribution of *IL6R* correlated well with *ACE2* in proximal tubule cells (**Fig. 5g, Extended**
320 **Data Fig. 5d**). In human kidney a similar co-expression pattern was detected (**Fig. 5h**).

321 Our observations suggest a potential positive feedback loop between IL6 and *ACE2*
322 expression that can exacerbate COVID-19 disease progression due to increased viral entry and
323 dissemination.

324

325

326 **DISCUSSION**

327

328 Mammalian tissues and organs are composed of many different cell types that can vary in
329 abundance and cell state. Tissue heterogeneity is only beginning to be unraveled thanks to
330 the advent of single-cell profiling technologies that allow us to precisely map transcriptomic
331 and epigenomic programs. These technologies are revolutionizing our view of human
332 physiology and disease. Great efforts are being made to generate the first version of both
333 human and murine atlases^{13, 37}. The mouse is among the most commonly used model
334 organisms in biomedical research but many developmental or pathological aspects are not
335 paralleled in human. Understanding tissue and organ complexity in species that are
336 phylogenetically close to humans is an unmet requirement.

337 In this study, we have generated a single-cell transcriptomic atlas of nine organs (liver,
338 kidney, lung, pancreas, neocortex, aorta, parotid gland, thyroid and peripheral blood) from
339 cynomolgus monkey. We used this dataset not only to provide fundamental information
340 about the cellular composition of the different tissues tested but also as a platform to dissect
341 the overall expression distribution of the SARS-CoV-2 entry receptor, *ACE2*, and its serine
342 protease coactivator *TMPRSS2*^{9, 10}. Interestingly, *ACE2* was expressed in multiple epithelial
343 tissues besides the lung, especially the kidney and liver. Other organs of epithelial origin such
344 as the gut have also been implicated in the pathogenesis of the disease³⁸. A consequence of
345 this is that the SARS2-CoV-2 virus could infect these organs too, which would explain some of
346 the reported clinical manifestations of COVID-19². By comparing our dataset with publicly
347 available human single-cell RNA-seq data, we have also uncovered significant differences in
348 cell subtypes expressing *ACE2* between human and monkey. We showed different expression
349 patterns for *ACE2* in the lung, where the highest levels were detected in ciliated cells in
350 monkey and pulmonary alveolar type 2 cells in human. Similarly, we observed marked
351 differences in liver, in which monkey hepatocytes displayed higher *ACE2* and a larger number
352 of positive cells compared to the human. We do not know whether these differences will

353 affect the pathogenesis of COVID-19 between these two species. Nevertheless, this is a
354 relevant finding considering that monkeys are a preferred model for studying the
355 effectiveness of drug treatments and of vaccines against the impending COVID-19 pandemic.

356 Through correlation analysis, we identified new potential mechanisms that could
357 facilitate ACE2-mediated viral infection, including genes previously unreported in the context
358 of SARS-CoV-2 that are involved in stimulating different types of immune responses. We
359 observed high expression of *IDO2* and *ANPEP* in kidney, liver and lung. Expression of these
360 genes can be further induced by viral infection and they have been reported to be immune
361 modulators and/or mediate viral entry^{31, 33}. These observations are relevant as they highlight
362 new potential therapeutic vulnerabilities in the current emergency. In this respect, a number
363 of inhibitors of ANPEP are currently being tested in several disease contexts and could serve
364 to prevent the immune cell exhaustion often observed in many severe COVID-19 cases³⁹.
365 Similarly, mesenchymal stem/stroma cells (MSC) have immunomodulatory functions that are
366 partly related to IDO2 production³¹. It is tempting, thus, to speculate that cell therapies based
367 on MSC delivery could ameliorate COVID-19 by normalizing immune function and preventing
368 cytokine storms⁴⁰.

369 Intriguingly, in our data, we see heterogenous expression of *ACE2* within the individual
370 cell subtypes in six out of the nine monkey organs that we analyzed, which is also the case in
371 the three human organs analyzed. In this regard, we noticed two different cell populations in
372 the kidney proximal tubule, one with higher *ACE2* expression than the other. We performed
373 single-cell ATAC-seq of this organ to understand whether this phenomenon has an epigenetic
374 basis. Analysis of open chromatin regions within the *ACE2* locus revealed the enrichment of
375 STAT1, STAT3 and IRF1 binding sites. These transcription factors have important immune
376 functions and are direct targets of tissue protective and innate immune responses such as
377 Interleukin-6 signaling pathway and interferons. Analysis of *IL6R* distribution showed broad
378 expression within different the *ACE2*⁺ organs in monkey and human. This suggests a link
379 between paracrine IL6 (e.g. secreted by stromal cells including tissue resident macrophages)
380 and enhanced *ACE2* expression across different organs. Higher and more widespread *ACE2*
381 expression could promote increased viral entry. This observation could be very relevant given
382 recent reports describing clinical trials with Tocilizumab, a monoclonal antibody used for IL6R
383 blockade in patients with rheumatoid arthritis⁴¹, for the treatment of COVID-19
384 (<http://www.chictr.org.cn/showprojen.aspx?proj=49409>). IL6 has been related to aging and

385 tissue damage⁴², and this may explain why elderly individuals and those with underlying
386 inflammatory conditions have more severe reactions to SARS-CoV-2 infection (**Fig. 6**).
387 Importantly, high IL6 levels have been detected in plasma from COVID-19 patients⁴³. In this
388 context, the proposed enhanced affinity of SARS-CoV-2 for ACE2 compared to SARS-CoV may
389 underlie the differences in the clinical course between the two diseases⁴⁴.

390 All these observations reveal new potential mechanisms for COVID-19, opening new
391 therapeutic avenues for disease management. However, caution should be exercised when
392 making decisions before additional experimental validation becomes available. Further
393 scrutiny of our datasets may provide new associations useful for understanding COVID-19,
394 and in general will be of utmost relevance for systematic comparisons aiming to understand
395 monkey and human tissue composition and disease vulnerabilities.

396

397 **METHODS**

398

399 **Ethics statement.**

400 This study was approved by the Institutional Review Board on Ethics Committee of BGI
401 (permit no. BGI-IRB19125).

402

403 **Collection of monkey tissues.**

404 A 6-year old female cynomolgus monkey was purchased from Huazhen Laboratory Animal
405 Breeding Centre (Guangzhou, China). The monkey was anesthetized with ketamine
406 hydrochloride (10 mg/kg) and barbiturate (40 mg/kg) administration before being euthanized
407 by exsanguination. Tissues were isolated and placed on the ice-cold board for dissection.
408 Whole organs including lung, kidney, pancreas, liver, brain, thyroid, parotid gland, and aorta
409 were cut into 5-10 pieces, respectively (50-200 mg/piece). Samples were then quickly frozen
410 in liquid nitrogen and stored until nuclear extraction was performed. PBMC were isolated
411 from heparinized venous blood using a Lymphoprep™ medium (STEMCELL Technologies,
412 #07851) according to standard density gradient centrifugation methods. PBMC were
413 resuspended in 90% FBS, 10% DMSO (Sigma Aldrich, #D2650) freezing media and frozen using
414 a Nalgene® Mr. Frosty® Cryo 1°C Freezing Container (Thermo Fisher Scientific, #5100-0001)
415 in a -80°C freezer for 24 hours before being transferred to liquid nitrogen for long-term
416 storage.

417

418 **Single-nucleus/cell suspension preparation.**

419 We isolated nuclei as previously described⁴⁵. Briefly, tissues were thawed, minced and added
420 to lysis buffer. Lysates were filtered and resuspended in cell resuspension buffer. Frozen
421 PBMC vials were rapidly thawed in a 37°C water bath for ~2 minutes, then quenched with 10
422 ml 37°C pre-warmed 1X phosphate-buffered saline (PBS, Thermo Fisher Scientific,
423 #10010031) supplemented with 10% FBS. PBMCs were centrifuged at 500 *R.C.F.* for 5 minutes
424 at room temperature. The supernatant was removed, and the cell pellet was resuspended in
425 3 ml 37°C pre-warmed 1X PBS containing 0.04% bovine serum albumin (BSA, Sangon Biotech,
426 A600903), passed through a 40 µm cell strainer (Falcon, #352340) and then centrifuged at
427 500 *R.C.F.* for 5 minutes at room temperature. Nuclei or cells were resuspended with cell
428 resuspension buffer at a concentration of 1,000 cells/µl for single-cell library preparation.

429

430 **Single-nucleus/cell RNA-seq.**

431 The DNBelab C Series Single-Cell Library Prep Set (MGI, #1000021082) was utilized as
432 previously described (Liu et al. 2019). In brief, single-nucleus/cell suspensions were used for
433 droplet generation, emulsion breakage, beads collection, reverse transcription, and cDNA
434 amplification to generate barcoded libraries. Indexed single-cell RNA-seq libraries were
435 constructed according to the manufacturer's protocol. The sequencing libraries were
436 quantified by Qubit™ ssDNA Assay Kit (Thermo Fisher Scientific, #Q10212). Single-cell ATAC-
437 seq libraries were prepared using DNBelab C Series Single-Cell ATAC Library Prep Set (MGI,
438 #1000021878). DNA nanoballs (DNBs) were loaded into the patterned Nano arrays and
439 sequenced on the ultra-high-throughput DIPSEQ T1 sequencer using the following read
440 length: 30 bp for read 1, inclusive of 10 bp cell barcode 1, 10 bp cell barcode 2 and 10 bp
441 unique molecular identifier (UMI), 100 bp of transcript sequence for read 2, and 10 bp for
442 sample index.

443

444 **Single-cell RNA-seq data processing.**

445 Raw sequencing reads from DIPSEQ-T1 were filtered and demultiplexed using PISA (version
446 0.2) (<https://github.com/shiquan/PISA>). Reads were aligned to *Macaca fascicularis*_5.0
447 genome using STAR (version 2.7.4a)⁴⁶ and sorted by sambamba (version 0.7.0)⁴⁷. Cell versus
448 gene UMI count matrix was generated with PISA.

449

450 **Cell clustering and identification of cell types.**

451 Clustering analysis of the complete cynomolgus monkey tissue dataset was performed using
452 Scanpy (version 1.4)⁴⁸ in a Python environment. Parameters used in each function were
453 manually curated to portray the optimal clustering of cells. In preprocessing, cells or nuclei
454 were filtered based on the criteria of expressing a minimum of 200 genes and a gene which
455 is expressed by a minimum of 3 cells or nuclei. Filtered data were $\ln(\text{counts per million (CPM)}/100 + 1)$
456 transformed. 3000 highly variable genes were selected according to their
457 average expression and dispersion. The number of UMI and the percentage of mitochondrial
458 gene content were regressed out and each gene was scaled by default options. Dimension
459 reduction starts with principal component analysis (PCA), and the number of principal
460 components used for UMAP depends on the importance of embeddings. The Louvain method

461 is then used to detect subgroups of cells. Distinguishing differential genes among clusters
462 were ranked (Benjamini-Hochberg, Wilcoxon rank-sum test). Cell types were manually and
463 iteratively assigned based on overlap of literature, curated and statistically ranked genes.
464 Each tissue dataset was portrayed using the Seurat package (version 3.1.1)⁴⁹ in R environment
465 by default parameters for filtering, data normalization, dimensionality reduction, clustering,
466 and gene differential expression analysis. Finally, we annotated each cell type by extensive
467 literature reading and searching for the specific gene expression pattern.

468

469 **Gene correlation and Gene Ontology (GO) term enrichment analysis.**

470 The correlation between *ACE2* and other genes was drawn using Pearson correlation
471 coefficient (PCC) with gene expression value merged from cells of the same cell types with
472 the R package psych (version 1.9.12.31). To infer the biological function of highly correlated
473 genes ($cor > 0.6$ and adjusted P value < 0.001), we performed gene set enrichment analysis
474 using Metascape (<https://metascape.org/gp/index.html>).

475

476 **Differential gene expression analysis.**

477 Differential expression analysis between proximal tubule S1 and proximal tubule S3 was
478 performed using the FindMarkers function of the Seurat package (version 3.1.1).

479

480 **Single-cell ATAC-seq data processing.**

481 Raw sequencing reads from DIPSEQ-T1 were filtered and demultiplexed using PISA (version
482 0.2) (<https://github.com/shiquan/PISA>). Peak calling was performed using MACS2 (version
483 2.1.2)⁵⁰ with options `-f BAM -B -q 0.01 --nomodel`. The cell versus peak reads count matrix was
484 generated by custom script. To create a gene activity matrix, we extracted gene coordinates
485 for cynomolgus monkey from NCBI, and extended them to ± 2 kb region around TSS. The gene
486 activity score matrix was calculated by custom script.

487

488 **Single-cell ATAC-seq cell clustering and cell type identification.**

489 Cells with low fragments ($< 1,000$) and TSS proportion (< 0.1) were removed. Then, filtered
490 data were imported into R and the dimensionality was reduced by latent semantic indexing.
491 Anchors between single-cell ATAC-seq and single-cell RNA-seq datasets were identified and
492 used to transfer cell type labels identified from the single-cell RNA-seq data. We embedded

493 the single-cell ATAC-seq and single-cell RNA-seq data by the TransferData function of Seurat
494 (version 3.1.1).

495

496 **Transcription factor motif enrichment analysis.**

497 To predict the motif footprint in peaks within the *ACE2* promoter, we extracted genome
498 sequences in the peak region with Seqkit (version 0.7.0)⁵¹. The sequences were imported into
499 R and were matched with all *Homo sapiens* motifs from JASPAR2018 using matchMotifs
500 function in motifmatchr packages version 1.8.0 with default parameter.

501

502 **Human single-cell RNA-seq datasets.**

503 All human single-cell RNA-seq data matrix were obtained from publicly available dataset as
504 described: (1) Kidney data from Stewart et al. was download from
505 <https://www.kidneycellatlas.org/>⁵²; (2) Lung data from Madisson et al. was download from
506 <https://www.tissuestabilitycellatlas.org/>⁵³; (3) Liver data from Aizarani et al. was download
507 from GEO at accession GSE124395⁵⁴.

508

509 **Code availability**

510 Computer code used for processing the single-cell RNA-seq and single-cell ATAC-seq will be
511 available at <https://github.com/brucepan10/NHP-COVID-19>.

512

513 **Data availability**

514 All raw data have been deposited to CNGB Nucleotide Sequence Archive (accession code:
515 CNP0000986; <https://db.cngb.org/cnsa/project/CNP0000986/public/>)

516

517

518 **ACKNOWLEDGEMENTS**

519

520 We thank Xiaoyun Huang and Miaomiao Jiang of the Zhiyu Center for Systems Biology, Zhiyu
521 Inc., Shenzhen for their support. This work was supported by National Natural Science
522 Foundation of China (31900466, 31900582), Research and Development Program of China
523 (2018YFA0106903), the Strategic Priority Research Program of the Chinese Academy of
524 Sciences (XDA16030502) and CAS-JSPS Joint Research Projects (GJHZ2093), Natural Science

525 Foundation of Guangdong Province, China (2018A030313379), the Shenzhen National Key
526 Laboratory of Single-Cell Omics (ZDSYS20190902093613831) and Shenzhen Bay Laboratory
527 (SZBL2019062801012). G.V. is supported by Chinese Academy of Sciences President's
528 International Fellowship for Foreign Experts (2020FSB0002). C.W. is supported by Chinese
529 Academy of Sciences President's International Fellowship Initiative for Postdoctoral
530 Researchers (2019PB0177) and Research Fund for International Young Scientists grant
531 (31950410553). This work is part of the South China Greater Bay Area-Single Cell Consortium
532 under the coordination of M.A.E, L.L., X.X. and Y.H.. This publication is part of the Human Cell
533 Atlas - www.humancellatlas.org/publications/.

534

535

536 **AUTHOR CONTRIBUTIONS**

537

538 L.L., M.A.E., Y.H. and X.X. conceived the idea. L.L., L.H., Y.L., S.L., X.W. and Y.Yuan. designed
539 the experiment. L.H., Y.L., S.L., X.W., Y.Y., M.C. and C.W.W. collected the tissue samples. C.L.,
540 Z.W., Y.Yuan, Y. Yu, M.W., T.W., Y.L., C.W., Y.Z., T.T., Y.H., H.L., L.X., J.X. and M.C. performed
541 the experiments. X.W., T.P., Q.S., L.W., Z.Z., Y.L., S.Z. and S.L. performed the data analysis.
542 L.L., L.H., X.W., C.L., G.V., T.P., C.W. and Y.L. prepared the figures. P.H.M provided critical
543 review of the manuscript. M.A.E., G.V., C.W., Y.L. and L.L. wrote the manuscript with input
544 from all authors. X.X., Y.H., L.L. and M.A.E supervised the entire study. All other authors
545 contributed to the work. All authors read and approved the manuscript for submission.

546

547

548 **COMPETING INTERESTS**

549

550 Employees of BGI have stock holdings in BGI.

551

552 **FIGURE LEGENDS**

553

554 **Fig. 1 | Construction of single-cell atlas across nine tissues of a *Macaca fascicularis* monkey.**

555 **a**, Schematic representation of selected monkey tissues used in this study and description of
556 experimental pipeline for the single-cell sequencing.

557 **b**, UMAP visualization of all single cells from the dataset colored by tissue/organ (left) and
558 number of cells from each tissue passing quality control (right).

559 **c**, UMAP visualization of each cell type colored according to 44 clusters in the first round of
560 clustering. Cell type annotation is provided in the figure and is associated with a number
561 indicative of every cluster. $n = 215,334$ individual nuclei/cells.

562

563 **Fig. 2 | *ACE2* and *TMPRSS2* expression across 44 cell clusters in monkey.**

564 **a-b**, UMAP projection of *ACE2* (**a**) and *TMPRSS2* (**b**) expression in all single cells within our
565 dataset.

566 **c**, UMAP projection of *ACE2*⁺/*TMPRSS2*⁺ cells.

567 **d**, Bubble plots showing the level of expression of *TMPRSS2* and *ACE2* genes and the ratio of
568 expressing cells in the indicated cell types. The color of each bubble represents the level of
569 expression and the size indicates the proportion of expressing cells.

570 **e**, Barplot indicating the percentage of *ACE2* and *TMPRSS2* expressing cells within each cell
571 cluster.

572

573 **Fig. 3 | Comparative analysis of *ACE2* and *TMPRSS2* expression between monkey and
574 human.**

575 **a-c**, UMAP projection of *ACE2* (top) and *TMPRSS2* (bottom) expression in single cells of
576 monkey lung (**a**), kidney (**b**) and liver tissues (**c**). The red arrow in this panel indicates
577 cholangiocytes. The color of the cells reflects the expression level as indicated in the scale
578 bar. **d-f**, Bubble plots showing the ratio and expression of *ACE2* and *TMPRSS2* in the indicated
579 cell types of lung (**d**), kidney (**e**) and liver (**f**) in monkey and human. The color of each bubble
580 represents the level of expression and the size indicates the proportion of expressing cells.

581

582 **Fig. 4 | Co-expression analysis of *ACE2* in monkey tissues.**

583 **a**, Volcano plot of correlation coefficients (Pearson r^2) from association tests between *ACE2*
584 and other individual genes. The correlation coefficient for every gene (x-axis) versus the
585 adjusted *P* value (using Benjamini-Hochberg correction; y-axis). The genes indicated in the
586 plot are those with a correlation score > 0.6 and an adjusted *P*-value < 0.001 .

587 **b**, Gene ontology analysis of genes that show high expression correlation with *ACE2*.

588 **c**, Scatter plots showing the association between *ACE2* and the indicated genes. The
589 correlation coefficients (Pearson r^2) and adjusted *P* values are shown in the plots.

590 **d**, UMAP projection of expression of the indicated genes in all single cells.

591

592 **Fig. 5 | Chromatin accessibility analysis reveals epigenetic regulation of *ACE2* in kidney.**

593 **a**, Schematic of experimental design for single-cell ATAC-seq of monkey.

594 **b**, Joint UMAP visualization of kidney single-cell ATAC (scATAC)-seq data with single-cell RNA
595 (scATAC)-seq data. **c**, UMAP visualization of single-cell ATAC-seq data.

596 **d**, IGV visualization of aggregate single-cell ATAC-seq signal in each cell type.

597 **e**, Ratio of *ACE2*⁺ cells in each cell type of kidney.

598 **f**, The transcription factor motifs predicted based on DNA sequence within those regions of
599 the *ACE2* locus.

600 **g-h**, UMAP projection of *IL6R* expression and cells with *IL6R*⁺/*ACE2*⁺ cells in all kidney single
601 cell in monkey (**g**) and human (**h**).

602

603 **Fig. 6 | Proposed molecular mechanism for SARS-Cov-2 pathogenesis through reinforced**
604 **IL6-mediated immune response in monkey and humans.**

605 Schematic representation of potential mechanism of SARS-CoV-2 spreading through lung,
606 kidney and liver. Kidney proximal tubule cells within the nephron have the highest expression
607 of ACE2 receptor which facilitates virus entry. After virus contact, IL6R stimulates an immune
608 response that, through the activation of STAT factors, potentiates the paracrine positive
609 feedback loop that facilitates virus spreading. IL6 expression, which is higher in elderly
610 patients and those with inflammatory conditions, is effectively targeted by anti-IL6R
611 monoclonal antibodies leading to a more favourable disease course.

612

613

614

615 **EXTENDED DATA FIGURE LEGENDS**

616

617 **Extended Data Fig. 1 | Quality control of the single-cell RNA-seq libraries.**

618 **a**, Violin plot showing the number of unique molecular identifiers (UMIs) identified in each
619 tissue.

620 **b**, Violin plot showing the number of genes identified in each organ. **(C)** Heatmap showing the
621 expression of marker genes of the indicated cell type

622

623 **Extended Data Fig. 2 | Various cell types identified in each tissue.**

624 **a-i**, UMAP visualization of cell clusters in lung **(a)**, kidney **(b)**, liver **(c)**, PBMC **(d)**, neocortex
625 **(e)**, parotid **(f)**, aorta **(g)**, thyroid **(h)** and pancreas **(i)**. The name of the population
626 corresponding to each cell cluster is indicated in every plot.

627

628 **Extended Data Fig. 3 | *ACE2* and *TMPRSS2* expression in each tissue.**

629 **a-b**, UMAP Projection of *ACE2* **(a)** and *TMPRSS2* **(b)** expression in each tissue.

630

631 **Extended Data Fig. 4 | Spatially specific subclusters of proximal tubule cells in monkey**
632 **kidney.**

633 **a**, UMAP visualization of single cells from the kidney tissue, colored by cell types.

634 **b**, Volcano plot showing the differentially expressed genes between proximal tubule S1 and
635 proximal tubule S3 cells. Examples of highly variable genes are indicated.

636 **c**, UMAP projection of expression for the indicated genes in all single cells.

637 **d**, The structure and specific gene expression in kidney tubules. The specific genes and *ACE2*
638 expression level for proximal tubule S1 and proximal tubule S3 cells are indicated.

639

640 **Extended Data Fig. 5 | Quality control of single-cell ATAC-seq data.**

641 **a**, Number of fragments captured in all cells of the two single-cell ATAC-seq libraries.

642 **b**, Proportion of TSS fragments in all cells of the two single-cell ATAC-seq libraries.

643 **c**, IGV visualization of specific accessible chromatin in each cell type.

644 **d**, UMAP projection of *ACE2* expression in human kidney.

645

646

647 **REFERENCES**

648

- 649 1. Kock, R.A., Begovoeva, M., Ansumana, R. & Suluku, R. Searching for the source of
650 Ebola: the elusive factors driving its spillover into humans during the West African
651 outbreak of 2013-2016. *Rev Sci Tech* **38**, 113-122 (2019).
- 652 2. Zhu, N. *et al.* A Novel Coronavirus from Patients with Pneumonia in China, 2019. *The*
653 *New England journal of medicine* **382**, 727-733 (2020).
- 654 3. Cui, J., Li, F. & Shi, Z.L. Origin and evolution of pathogenic coronaviruses. *Nat Rev*
655 *Microbiol* **17**, 181-192 (2019).
- 656 4. Su, S. *et al.* Epidemiology, Genetic Recombination, and Pathogenesis of Coronaviruses.
657 *Trends Microbiol* **24**, 490-502 (2016).
- 658 5. Lau, S.K. *et al.* Severe acute respiratory syndrome coronavirus-like virus in Chinese
659 horseshoe bats. *Proc Natl Acad Sci U S A* **102**, 14040-14045 (2005).
- 660 6. Reusken, C.B. *et al.* Middle East respiratory syndrome coronavirus neutralising serum
661 antibodies in dromedary camels: a comparative serological study. *Lancet Infect Dis* **13**,
662 859-866 (2013).
- 663 7. Chan, J.F. *et al.* A familial cluster of pneumonia associated with the 2019 novel
664 coronavirus indicating person-to-person transmission: a study of a family cluster.
665 *Lancet* **395**, 514-523 (2020).
- 666 8. Rothe, C. *et al.* Transmission of 2019-nCoV Infection from an Asymptomatic Contact
667 in Germany. *The New England journal of medicine* **382**, 970-971 (2020).
- 668 9. Hoffmann, M. *et al.* SARS-CoV-2 Cell Entry Depends on ACE2 and TMPRSS2 and Is
669 Blocked by a Clinically Proven Protease Inhibitor. *Cell* **181**, 271-280 (2020).
- 670 10. Walls, A.C. *et al.* Structure, Function, and Antigenicity of the SARS-CoV-2 Spike
671 Glycoprotein. *Cell*, Epub ahead of print (2020).
- 672 11. Rockx, B. *et al.* Comparative pathogenesis of COVID-19, MERS, and SARS in a
673 nonhuman primate model. *Science*, Epub ahead of print (2020).
- 674 12. Bao, L. *et al.* Reinfection could not occur in SARS-CoV-2 infected rhesus macaques.
675 *bioRxiv*, 2020.2003.2013.990226 (2020).
- 676 13. Han, X. *et al.* Construction of a human cell landscape at single-cell level. *Nature* (2020).
- 677 14. Hamming, I. *et al.* Tissue distribution of ACE2 protein, the functional receptor for SARS
678 coronavirus. A first step in understanding SARS pathogenesis. *J Pathol* **203**, 631-637
679 (2004).
- 680 15. Naicker, S. *et al.* The Novel Coronavirus 2019 epidemic and kidneys. *Kidney Int* (2020).
- 681 16. Conti, P. *et al.* Induction of pro-inflammatory cytokines (IL-1 and IL-6) and lung
682 inflammation by Coronavirus-19 (COVI-19 or SARS-CoV-2): anti-inflammatory
683 strategies. *J Biol Regul Homeost Agents* **34** (2020).
- 684 17. Bagheri, S.H.R. *et al.* Coincidence of COVID-19 epidemic and olfactory dysfunction
685 outbreak. *medRxiv*, 2020.2003.2023.20041889 (2020).
- 686 18. Liu, C. *et al.* A portable and cost-effective microfluidic system for massively parallel
687 single-cell transcriptome profiling. *bioRxiv*, 818450 (2019).
- 688 19. Turner, A.J., Hiscox, J.A. & Hooper, N.M. ACE2: from vasopeptidase to SARS virus
689 receptor. *Trends Pharmacol Sci* **25**, 291-294 (2004).
- 690 20. Kim, T.S., Heinlein, C., Hackman, R.C. & Nelson, P.S. Phenotypic analysis of mice lacking
691 the Tmprss2-encoded protease. *Mol Cell Biol* **26**, 965-975 (2006).

- 692 21. Jia, H.P. *et al.* ACE2 receptor expression and severe acute respiratory syndrome
693 coronavirus infection depend on differentiation of human airway epithelia. *J Virol* **79**,
694 14614-14621 (2005).
- 695 22. Li, Z. *et al.* Caution on Kidney Dysfunctions of COVID-19 Patients. *medRxiv*,
696 2020.2002.2008.20021212 (2020).
- 697 23. Peiris, J.S. *et al.* Coronavirus as a possible cause of severe acute respiratory syndrome.
698 *Lancet* **361**, 1319-1325 (2003).
- 699 24. Hamm, H., Fabel, H. & Bartsch, W. The surfactant system of the adult lung: physiology
700 and clinical perspectives. *Clin Investig* **70**, 637-657 (1992).
- 701 25. Mason, R.J. & Williams, M.C. Type II alveolar cell. Defender of the alveolus. *Am Rev*
702 *Respir Dis* **115**, 81-91 (1977).
- 703 26. Lee, J.W., Chou, C.L. & Knepper, M.A. Deep Sequencing in Microdissected Renal
704 Tubules Identifies Nephron Segment-Specific Transcriptomes. *J Am Soc Nephrol* **26**,
705 2669-2677 (2015).
- 706 27. Santer, R. & Calado, J. Familial renal glucosuria and SGLT2: from a mendelian trait to
707 a therapeutic target. *Clin J Am Soc Nephrol* **5**, 133-141 (2010).
- 708 28. Yu, L. *et al.* Abnormal expression and dysfunction of novel SGLT2 mutations identified
709 in familial renal glucosuria patients. *Hum Genet* **129**, 335-344 (2011).
- 710 29. Chu, P.L. *et al.* Renal Collectrin Protects against Salt-Sensitive Hypertension and Is
711 Downregulated by Angiotensin II. *J Am Soc Nephrol* **28**, 1826-1837 (2017).
- 712 30. Sigdel, T.K. *et al.* Immune response profiling identifies autoantibodies specific to
713 Moyamoya patients. *Orphanet journal of rare diseases* **8**, 45 (2013).
- 714 31. Ball, H.J., Yuasa, H.J., Austin, C.J., Weiser, S. & Hunt, N.H. Indoleamine 2,3-
715 dioxygenase-2; a new enzyme in the kynurenine pathway. *The international journal of*
716 *biochemistry & cell biology* **41**, 467-471 (2009).
- 717 32. Lepiller, Q. *et al.* Antiviral and Immunoregulatory Effects of Indoleamine-2,3-
718 Dioxygenase in Hepatitis C Virus Infection. *J Innate Immun* **7**, 530-544 (2015).
- 719 33. Delmas, B. *et al.* Aminopeptidase N is a major receptor for the entero-pathogenic
720 coronavirus TGEV. *Nature* **357**, 417-420 (1992).
- 721 34. Wentworth, D.E. & Holmes, K.V. Molecular determinants of species specificity in the
722 coronavirus receptor aminopeptidase N (CD13): influence of N-linked glycosylation. *J*
723 *Virol* **75**, 9741-9752 (2001).
- 724 35. Guo, Y.R. *et al.* The origin, transmission and clinical therapies on coronavirus disease
725 2019 (COVID-19) outbreak - an update on the status. *Mil Med Res* **7**, 11 (2020).
- 726 36. Heinrich, P.C., Castell, J.V. & Andus, T. Interleukin-6 and the acute phase response. *The*
727 *Biochemical journal* **265**, 621-636 (1990).
- 728 37. Han, X. *et al.* Mapping the Mouse Cell Atlas by Microwell-Seq. *Cell* **172**, 1091-1107
729 e1017 (2018).
- 730 38. Ong, J., Young, B.E. & Ong, S. COVID-19 in gastroenterology: a clinical perspective. *Gut*,
731 Epub ahead of print (2020).
- 732 39. Zheng, M. *et al.* Functional exhaustion of antiviral lymphocytes in COVID-19 patients.
733 *Cell Mol Immunol*, Epub ahead of print (2020).
- 734 40. Wilson, J.G. *et al.* Mesenchymal stem (stromal) cells for treatment of ARDS: a phase 1
735 clinical trial. *Lancet Respir Med* **3**, 24-32 (2015).
- 736 41. Villiger, P.M. *et al.* Tocilizumab for induction and maintenance of remission in giant
737 cell arteritis: a phase 2, randomised, double-blind, placebo-controlled trial. *Lancet*
738 **387**, 1921-1927 (2016).

- 739 42. Mosteiro, L., Pantoja, C., de Martino, A. & Serrano, M. Senescence promotes in vivo
740 reprogramming through p16(INK)(4a) and IL-6. *Aging Cell* **17** (2018).
- 741 43. Wan, S. *et al.* Characteristics of lymphocyte subsets and cytokines in peripheral blood
742 of 123 hospitalized patients with 2019 novel coronavirus pneumonia (NCP). *medRxiv*,
743 2020.2002.2010.20021832 (2020).
- 744 44. Shang, J. *et al.* Structural basis of receptor recognition by SARS-CoV-2. *Nature* (2020).
- 745 45. Bakken, T.E. *et al.* Single-nucleus and single-cell transcriptomes compared in matched
746 cortical cell types. *PLoS One* **13**, e0209648 (2018).
- 747 46. Dobin, A. *et al.* STAR: ultrafast universal RNA-seq aligner. *Bioinformatics* **29**, 15-21
748 (2013).
- 749 47. Tarasov, A., Vilella, A.J., Cuppen, E., Nijman, I.J. & Prins, P. Sambamba: fast processing
750 of NGS alignment formats. *Bioinformatics* **31**, 2032-2034 (2015).
- 751 48. Wolf, F.A., Angerer, P. & Theis, F.J. SCANPY: large-scale single-cell gene expression
752 data analysis. *Genome Biol* **19**, 15 (2018).
- 753 49. Stuart, T. *et al.* Comprehensive Integration of Single-Cell Data. *Cell* **177**, 1888-
754 1902.e1821 (2019).
- 755 50. Feng, J., Liu, T., Qin, B., Zhang, Y. & Liu, X.S. Identifying ChIP-seq enrichment using
756 MACS. *Nat Protoc* **7**, 1728-1740 (2012).
- 757 51. Shen, W., Le, S., Li, Y. & Hu, F. SeqKit: A Cross-Platform and Ultrafast Toolkit for
758 FASTA/Q File Manipulation. *PLoS One* **11**, e0163962 (2016).
- 759 52. Stewart, B.J. *et al.* Spatiotemporal immune zonation of the human kidney. *Science* **365**,
760 1461-1466 (2019).
- 761 53. Madisson, E. *et al.* scRNA-seq assessment of the human lung, spleen, and esophagus
762 tissue stability after cold preservation. *Genome Biol* **21**, 1 (2019).
- 763 54. Aizarani, N. *et al.* A human liver cell atlas reveals heterogeneity and epithelial
764 progenitors. *Nature* **572**, 199-204 (2019).
- 765

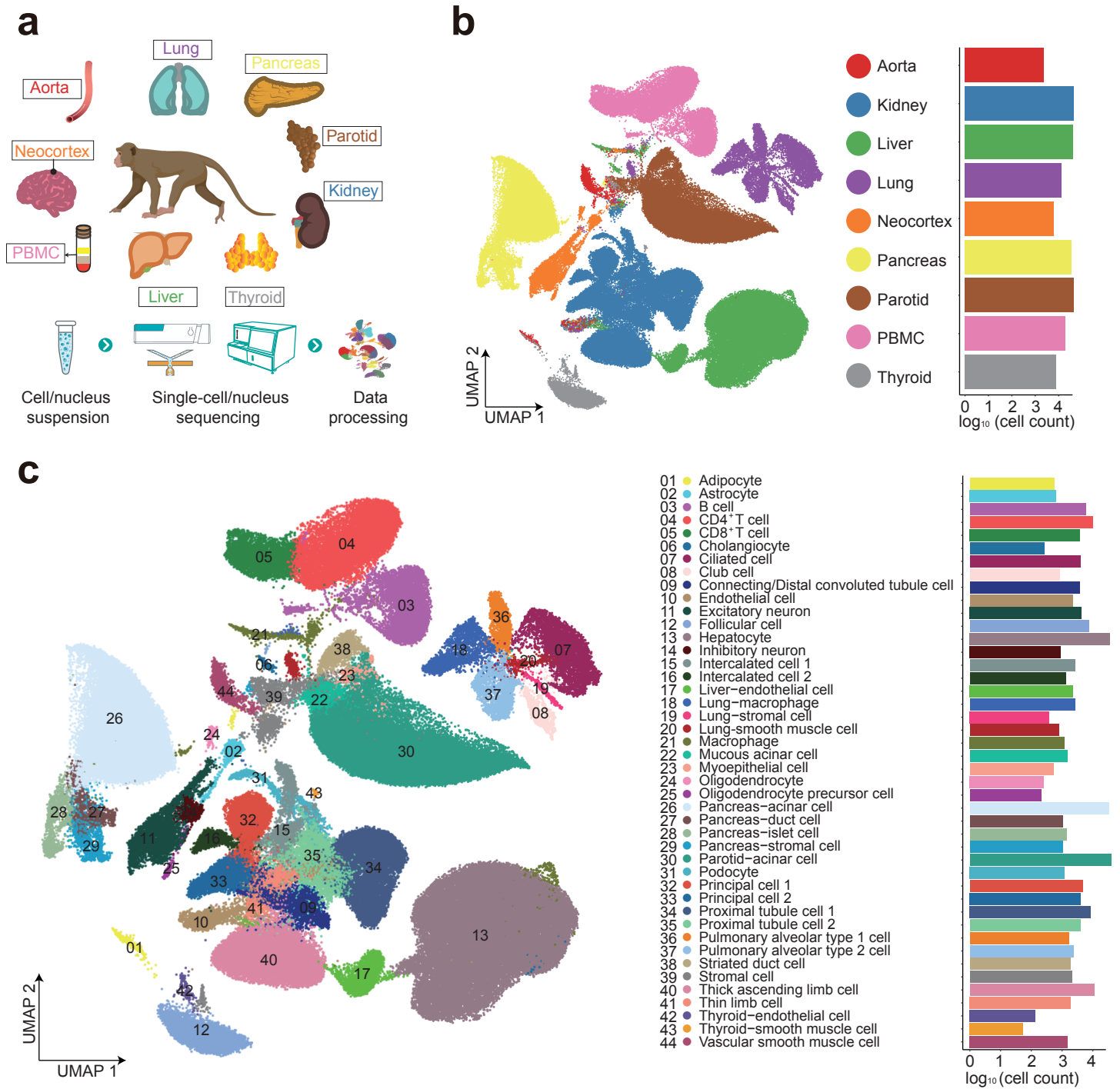


Figure 1

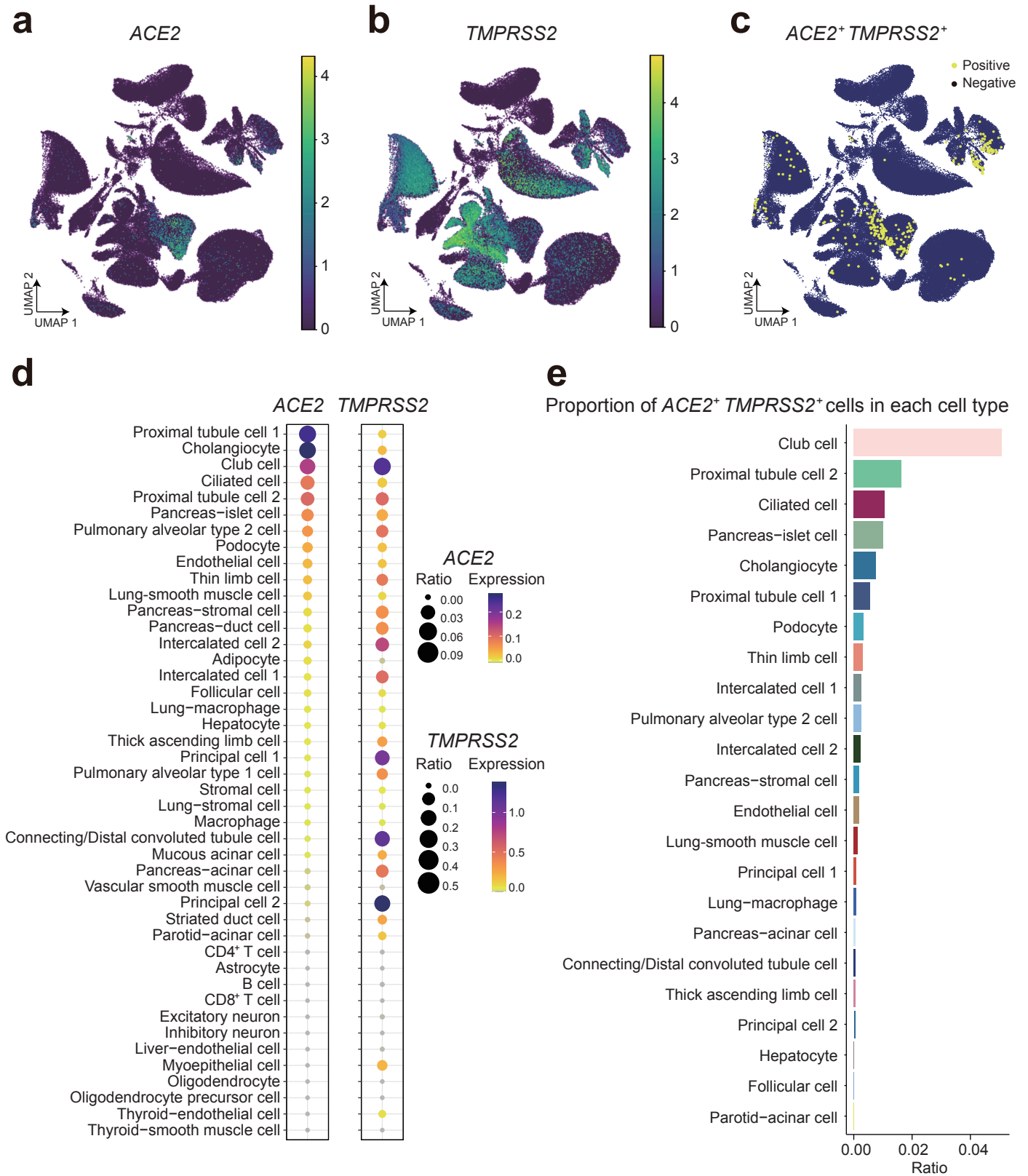


Figure 2

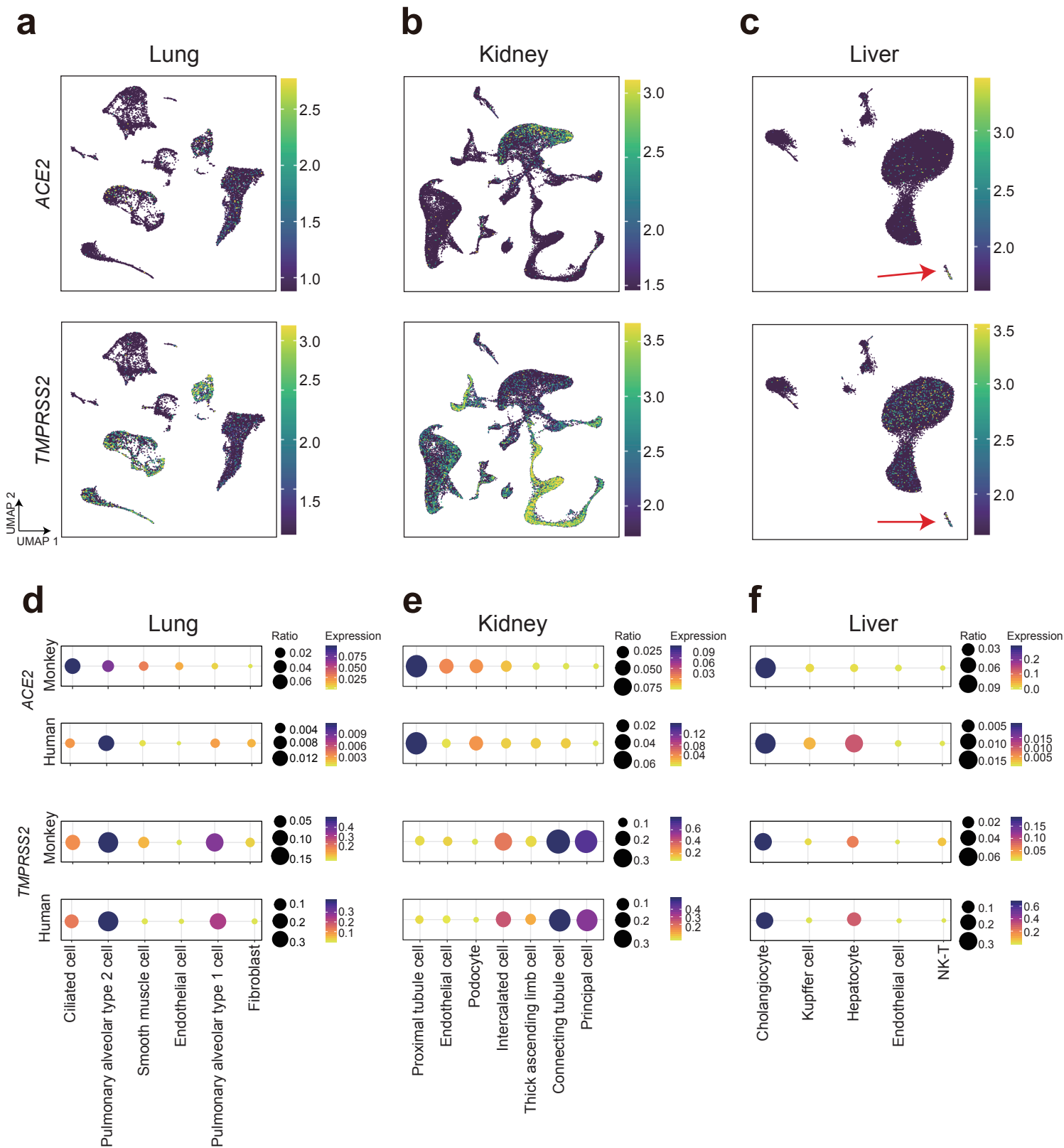
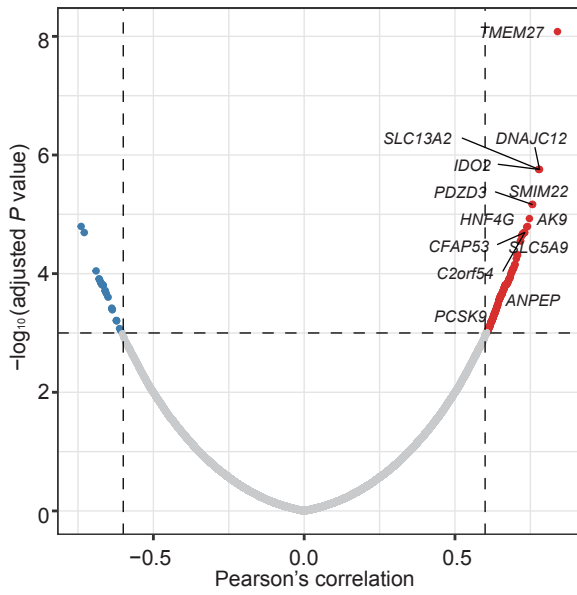
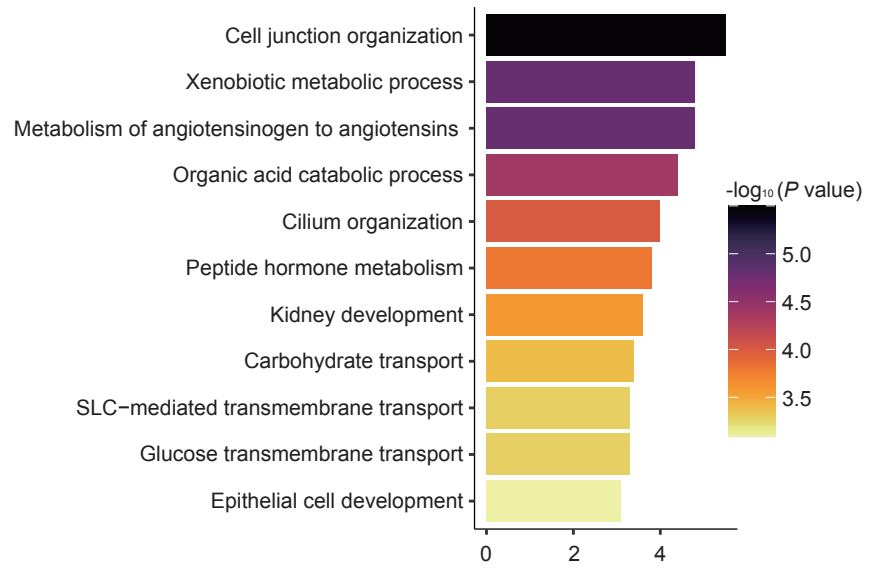


Figure 3

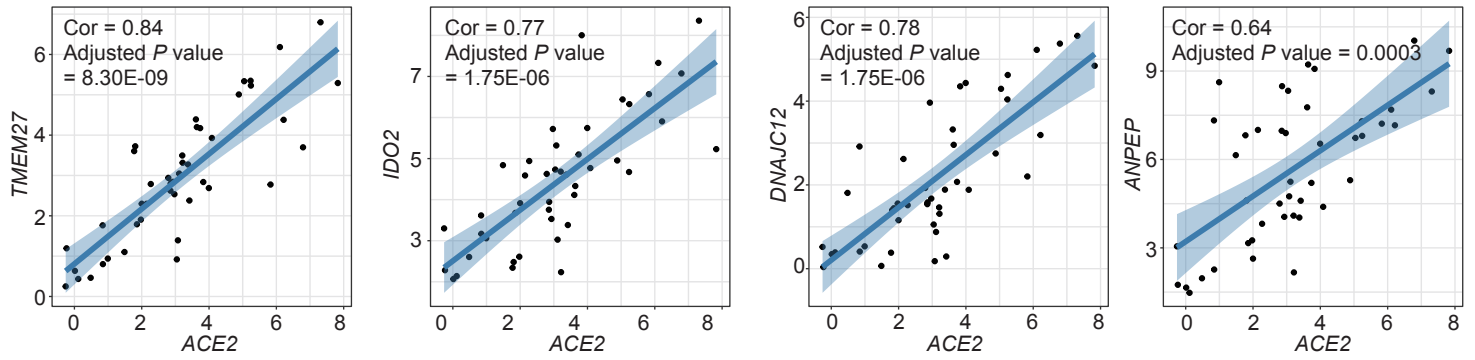
a



b



c



d

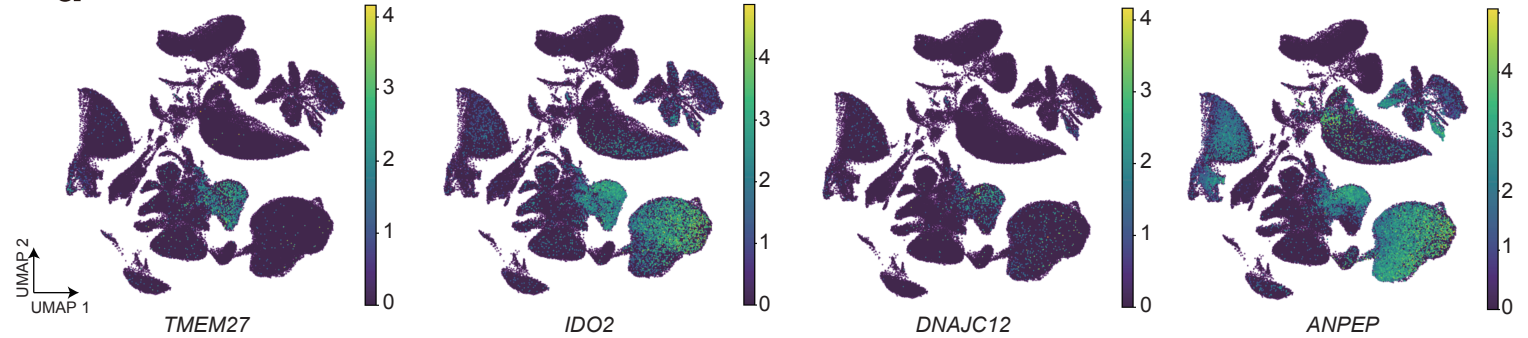


Figure 4

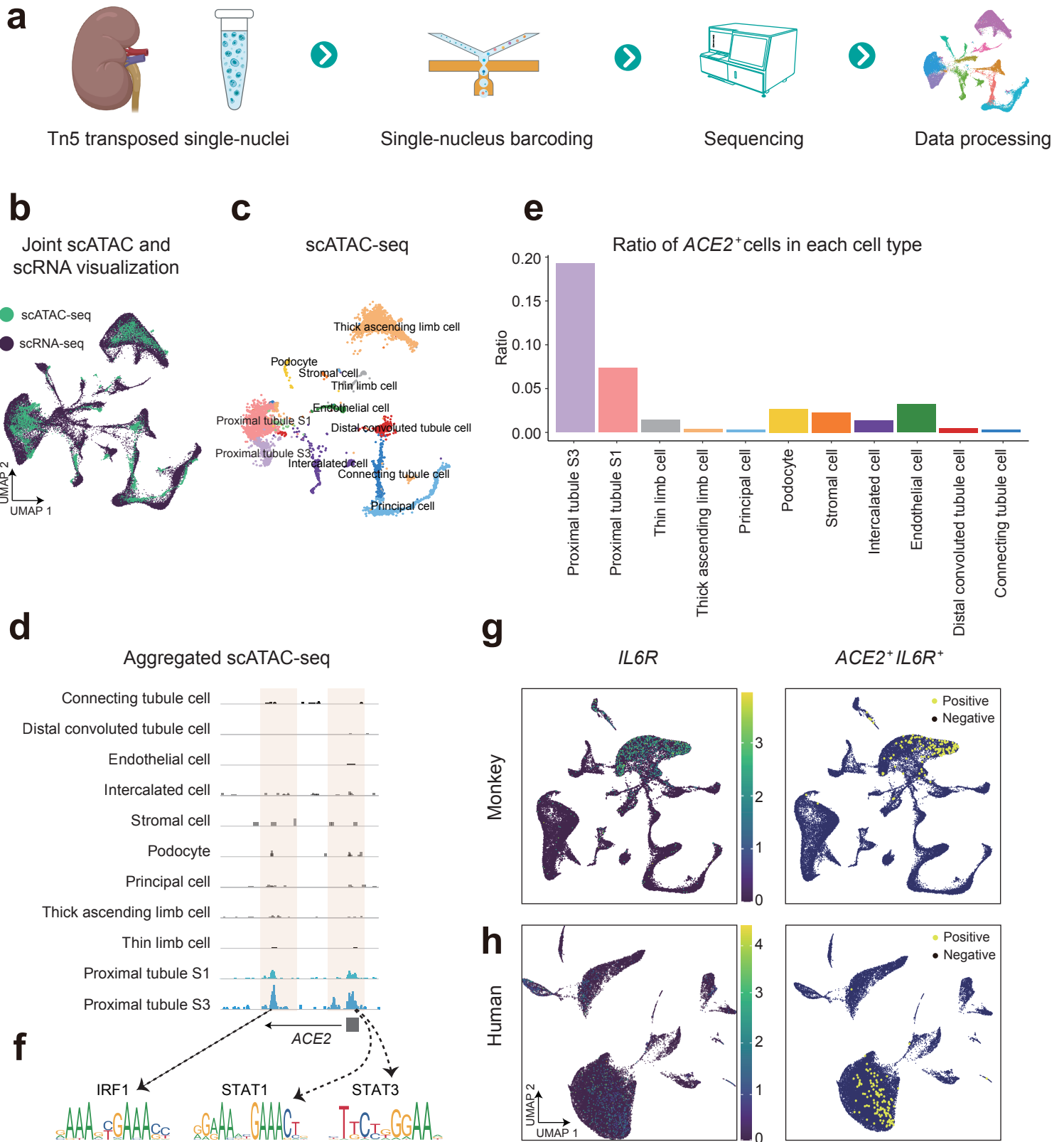


Figure 5

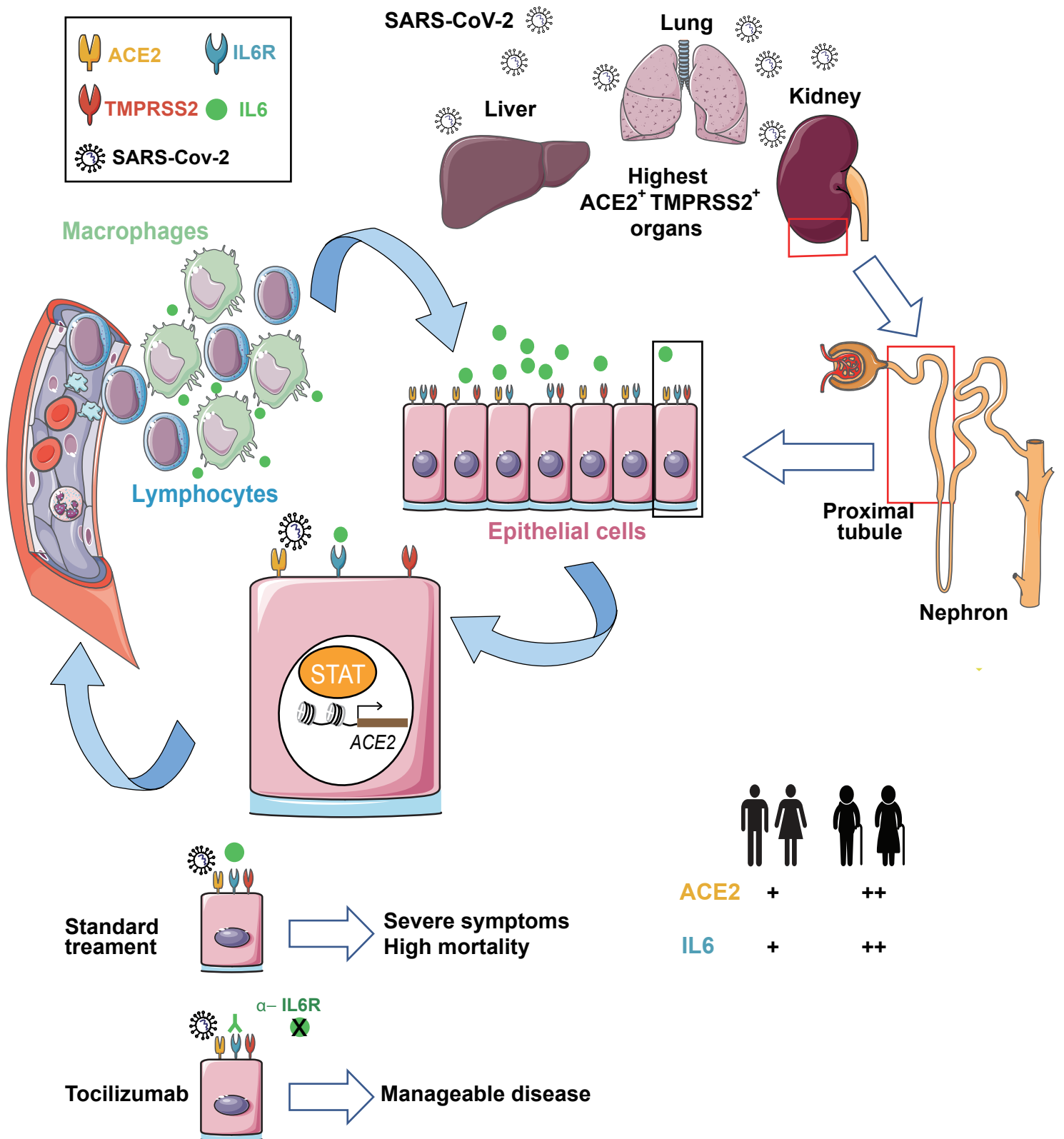


Figure 6

